



OPEN PCL scaffold with well-defined hierarchical pores effectively controls cell migration and alignment of human mesenchymal stem cells

Se-Hwan Lee¹, Jaeyeon Lee², Nae-Un Kang³, Yong Sang Cho⁴, Su Chin Heo^{1,5}, Yongdoo Park²✉ & Young-Sam Cho^{6,7}✉

With an increasing incidence of orthopedic fractures due to the growing aging population, the demand for novel bone tissue engineering treatments is rising. Existing biopolymeric scaffolds have hierarchical structure, are biocompatible, and are biodegradable, but struggle to control pore size and interconnectivity, essential features to regulate cell alignment and mechanobiological signaling. This highlights the need to design a biopolymeric scaffold with well-defined hierarchical structure and optimized surface properties to improve bone regeneration. To accomplish this, we proposed a grid-in-grid manufacturing approach and fabricated a solvent-free 3D polycaprolactone (PCL) scaffold with hierarchical pores using precision extruding deposition (PED) 3D printing technology. The fabricated scaffolds exhibit both global pores and multi-scale local pores. Notably, using *in vitro* cultured human mesenchymal stem cells (hMSCs), controlled local pore size induced contact guidance and pore bridging, and the surface roughness of global strands effectively led to cell alignment. This study demonstrates that precision 3D printing technology can directly manipulate local pore structures to control cell migration and alignment. Furthermore, it could be applied for combined bone to connective tissue regeneration, where gradient pore structures and cell alignment are essential. Our scaffold has the potential to serve as a customizable platform for advanced tissue engineering applications.

Keywords Hierarchical scaffold, Cell alignment, Precision extruding deposition head, Polycaprolactone, Solvent free

With the aging global population, there has been a marked increase in orthopedic fractures and associated bone fractures¹. Bone tissue possesses a natural capacity for self-repair and regeneration, enabling minor defects to heal without the need for surgical intervention². However, if a defect exceeds the critical size (usually 2 cm or more than half of the bone circumference) nonunion, malunion, or pathologic fracture may occur, which require surgery^{3,4}. Approximately 4 million people worldwide require bone grafting or replacement surgery each year, and common methods include autografts, allografts, and xenografts to restore defective or degenerative bone tissue^{5,6}. Autografts require an additional surgical procedure for tissue harvesting, leading to prolonged operative time and recovery periods. This increases the risk of infection and imposes a greater burden on the

¹McKay Orthopaedic Research Laboratory, Department of Orthopaedic Surgery, Perelman School of Medicine, University of Pennsylvania, Philadelphia, PA 19104, USA. ²Department of Biomedical Engineering, College of Medicine, Korea University, 73 Incheon-ro, Seongbuk-gu, Seoul 02841, Republic of Korea. ³Department of Mechanical Engineering, College of Engineering, Wonkwang University, Iksan 54538, Republic of Korea. ⁴Medical Device Development Center, Daegu-Gyeongbuk Medical Innovation Foundation (K-MEDI hub), Daegu 41061, Republic of Korea. ⁵Translational Musculoskeletal Research Center, Corporal Michael J Crescenz VA Medical Center, Philadelphia, PA 19104, USA. ⁶Division of Mechanical Engineering, College of Engineering, Wonkwang University, 460, Iksandae-ro, Iksan 54538, Jeonbuk, Republic of Korea. ⁷MECHABIO Group, Wonkwang University, Iksan 54538, Republic of Korea. ✉email: ydpark67@korea.ac.kr; youngsamcho@wku.ac.kr

patient. Additionally, xenografts present limitations such as immune rejection and a heightened risk of secondary infections^{7,8}. Therefore, current approaches have important drawbacks that need to be considered.

A developing alternative to these surgical methods is tissue engineering scaffolds for bone regeneration. In bone tissue engineering, scaffolds are fabricated with material properties and architectures to serve as structural supports for cells and promote tissue regeneration. Synthetic biopolymers such as polycaprolactone (PCL) are used for 3D porous scaffold fabrication because of their excellent mechanical property. We chose the PCL for our design because it is Food and Drug Administration (FDA) approved and exhibits many desirable qualities of an implantable material⁹. Namely, it is biocompatible, affordable, easy to fabricate, triggers a minimal immune response, and has a slow degradation rate, making it suitable for bone load-bearing applications¹⁰.

For our scaffold architecture to promote integration and new tissue formation *in vivo*, it must mimic native bone architecture as well as facilitate cell adhesion, proliferation and extracellular matrix (ECM) production^{11,12}. Scaffold porosity and surface area are key parameters that must be optimized to promote tissue regeneration. High porosity supports cell growth by ensuring nutrient transport, while a large surface area supports cell attachment and improves scaffold degradation rates¹³. Pore sizes are typically between 200 μm to 1000 μm for bone tissue regeneration, with smaller pores promoting faster tissue growth and larger pores supporting nutrient transport^{14–16}. Moreover, A high surface area is advantageous for cell attachment. Thus, pore size and surface area are crucial factors in determining the functionality of the scaffold.

Additive manufacturing, such as 3D printing, is used for scaffold fabrication because it enables replicable production of complex geometries, while reducing associated costs¹⁷. Two commonly used 3D printing technologies with high resolution for scaffold fabrication with polymers are photopolymerization and material extrusion¹⁸. While the photopolymerization method offers high precision, its drawback lies in the potential cytotoxic effects of uncured resin monomers and additives, which can adversely impact cells and tissues¹⁹. The extrusion-based methods melt thermoplastic polymers and extrude them under pressure, allowing for a solvent-free approach and making it safer to implant than photopolymerized scaffolds. Our material extrusion platform, a precision extrusion deposition (PED) head system, leverages this principle to enable the fabrication of high-resolution 3D structures using polycaprolactone (PCL) for complex bone defects. PED manufacturing allows for the highly controlled deposition of thermoplastics through a 50 μm inner diameter nozzle via a screw driven mechanical extrusion method⁹. Therefore, resulting scaffolds feature precise osteogenic geometries and are readily used for *in vivo* implantation.

One of the major obstacles in translating tissue engineering into clinical practice is the challenge of scaling up tissue engineered constructs for human therapy²⁰. The fabrication of 3D tissues necessitates the formation of vascular networks capable of delivering adequate nutrients and oxygen to sustain embedded cells²¹. However, the natural development of blood vessels within the tissue construct is typically not rapid enough to provide sufficient nutrient and oxygen supply after implantation, resulting in tissue necrosis²². To improve this, biodegradable scaffolds have been introduced in tissue engineering. Grid-structures are one of the most widely adopted designs for 3D porous scaffold fabrication. The repetitive linear design efficiently fabricates designed pores and produces uniform pores that provide interconnectivity of 3D structure, creating customizable 3D scaffolds. With sufficient grid pore size, nutrient transport can be achieved within the scaffolds. One challenge with this pattern is the cylindrical shape of the polymer strands when extruded through a circular nozzle. The low surface roughness and curvature of the circular strands provide a smooth surface (similar to a 2D tissue culture plate) for cells, which can influence cell morphology by allowing cell spreading and proliferation in all directions on the polymeric strand surface, making it difficult to control the cell alignment²³.

To mitigate this, scaffolds featuring hierarchical-structure have attracted considerable interest in improving the biological functions of 3D scaffold technology²⁴. Strand hierarchy allows for the creation of hierarchical topologies with a combination of small and large pores, giving rise to complex and large surfaces formed through the coexistence of numerous micro-pores ranging from tens to hundreds of micrometers in size¹⁵. Moreover, it effectively replicates the structural hierarchy of bone^{25,26}. Various methods have been reported to fabricate the hierarchical structure with the biopolymers, including 3D printing combined with gas foaming^{27,28}, 3D printing with particle leaching^{20,29,30}, 3D printing with phase separation³¹, molding with phase separation³², and molding with particle leaching³³, among others. Cho et al.³³ fabricated hierarchical PCL scaffolds using molding and particle leaching, demonstrating significantly enhanced cell attachment and proliferation compared to 3D-printed and particle-leached scaffolds with a single-pore system. Similarly, Feng et al.³⁴ used directional freezing technology to fabricate scaffolds with random, radial, and axial microchannel alignments, showing that aligned microchannels improved *in vivo* cell migration, infiltration, and osteochondral defect regeneration. These findings underscore the role of hierarchical structures in facilitating nutrient supply and waste removal while highlighting the importance of microchannel design in promoting superior regenerative outcomes. However, these methods still have limitations in controlling pore size and ensuring outstanding interconnectivity. Moreover, the biophysical cues imparted onto embedded cells still need to be considered. The cytoskeleton of the attached cells can be affected by physical cues of its substrate²³. Irregular surface geometrical characteristics can lead to random cellular morphology³⁵. Baker et al. showcased the feasibility of fibrocartilage engineering using nanofibrous scaffolds seeded with human stem cells, emphasizing the influence of microenvironmental factors and surface topography in MSC-based strategies^{36,37}. For these reasons, well-defined scaffold with surface properties that can control cell alignment and morphology are needed for mechanobiological strategies.

Here, we designed a well-defined hierarchical scaffold based on the concept of a multi-scale grid-structure scaffolds. Using the PED head-based precision 3D printing technology, we fabricated hierarchical PCL scaffolds by three-dimensionally stacking strands with a thickness of less than 85 μm and having local pores with multi-scale or linear wrinkle patterns. Building upon these scaffolds, we found that different patterns of predefined local strands regulate the migration and alignment of human mesenchymal stem cells (hMSCs). These advanced hierarchical scaffolds are designed to modulate cell behavior based on their high surface roughness and curvature,

providing a promising therapeutic strategy for large-area bone tissue damage, advancing tissue engineering and optimizing patient outcomes.

Results

Fabrication method for 3D scaffold with well-defined hierarchical pores

We defined a 3D structure composed of local pores and local strands as global strands, and representative design parameters were predefined for fabrication (Fig. 1a). Based on these parameters, a 3D global strand was fabricated using precision 3D printing with the PED head system (Fig. 1b), and the global strand was manufactured along the x-axis with predefined dimensions (Fig. 1c). This process was repeated along the z-axis with 90-degree rotated layers until a predefined height was reached (Fig. 1d). The resulting 3D scaffold had a well-defined hierarchical structure with global pores between global strands and local pores between local strands (Fig. 1e). This fabrication technology allows precise control over the size of local pores (Fig. 1f) and enables the production of a wrinkled surface, indicated by local peaks and troughs along strands, by adjusting the 3D pattern of local strands (Fig. 1g). The micro-wrinkle surface enhances the surface area and provides topographical cues to cells.

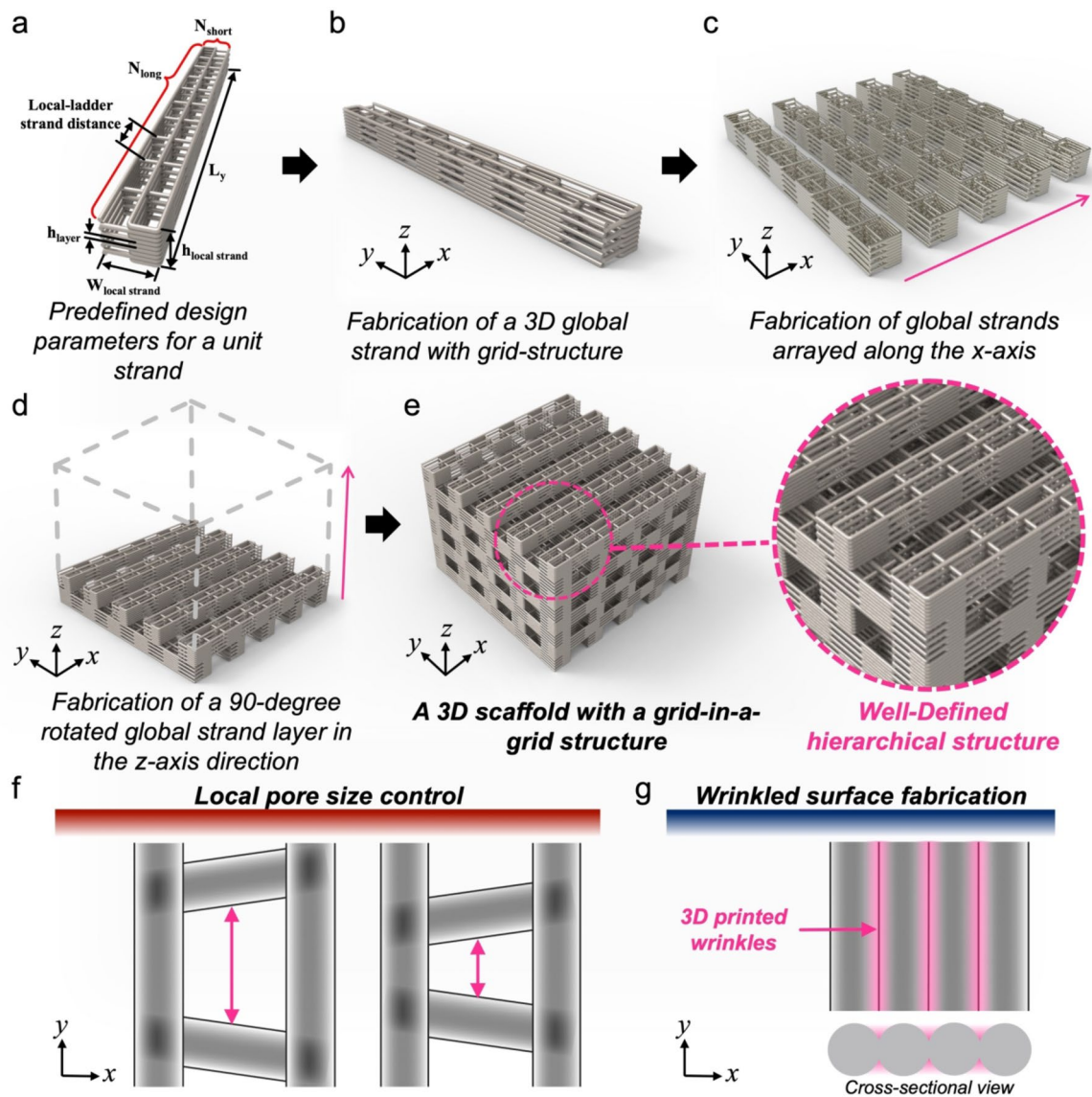


Fig. 1. Illustration of well-defined hierarchical scaffold by 3D printing with a precision extruding deposition (PED) head system: **(a)** Definition of design parameters for a unit strand, **(b)** Fabrication of a 3D unit strand with grid-structure design, **(c)** Fabrication of unit strands arrayed along the x-axis, **(d)** Process of stacking unit strand arrays in the z-axis, **(e)** 3D scaffold with a grid-in-grid structure design; **Schematic of representative local strand patterns fabricated using 3D patterning with the PED head:** **(f)** Local pore size control, **(g)** Wrinkled surface fabrication (This figures were partially created with BioRender.com; <https://BioRender.com/v25t132>, <https://BioRender.com/k99x570>).

	Local ladder-strand distance (μm)	Local pore	Micro-Wrinkles	Global pore
Group A	200, 150	+	Vertical	+
Group B	180, 100	+	Vertical	+
Group C	50	+	Vertical + Horizontal	+
Group D	-	-	-	+

Table 1. Experimental groups with structural feature.

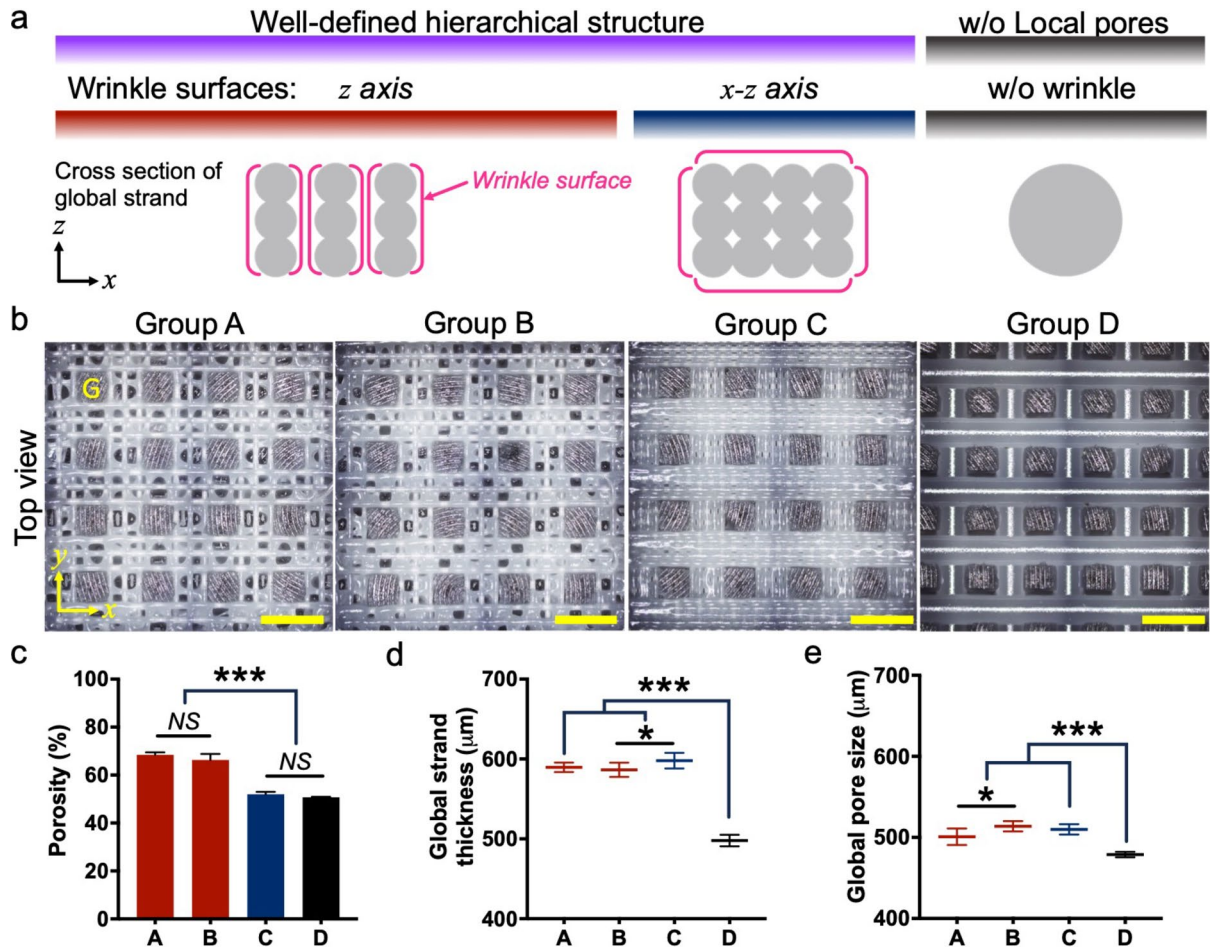


Fig. 2. Global scale features of the fabricated scaffold: (a) Classification of global strands; Fabricated PCL scaffold with well-defined hierarchical pores: (b) Optical microscopy images (Top view; G: Global pore; $\times 5$; scale bars: 1 mm); (c) Porosity of the scaffold ($n = 3$); (d) Global strand thickness ($n = 10$), (e) Global pore size ($n = 5$) (NS: Not significant, $*p < 0.05$, $***p < 0.001$).

Global scale morphology of the 3D scaffolds fabricated by precision 3D printing technology

Based on these controllable factors, the experimental groups were defined as follows: Group A = 200 μm and 150 μm local pore sizes, Group B = 180 μm and 100 μm local pore sizes, and Group C = 50 μm local pore size with a horizontal wrinkled surface (Table 1). Groups A and B were designed to have well-defined hierarchical structure with micro-rinkle surfaces only in the y-direction, whereas group C was designed to have wrinkles in both the x- and y-directions. In contrast, Group D was designed as a control group with a conventional scaffold, lacking surface wrinkles and hierarchical (local) pores (Fig. 2a). All groups were designed with a 500 μm global pore size and 50% global porosity.

Well-defined hierarchical scaffolds with various micro-pore characteristics were fabricated by 3D printing with a PED head (Fig. 2b and Supplementary Fig. S1a, b). The porosity of the fabricated scaffolds was Group A = 68.44 \pm 1.04%, Group B = 66.30 \pm 2.50%, Group C = 51.98 \pm 1.03%, and Group D = 50.74 \pm 1.04% (Fig. 2c). Group C was designed to have the same porosity for comparison with Group D, and the measured porosity of Group C scaffolds was similar to that of Group D. In addition, the porosities of Groups A and B, which had large scale-local pores, were found to be 34.88% and 30.67% higher than those of Groups C and D, respectively. The thickness of the global strand for each group was: Group A = 589.51 \pm 5.91 μm , Group B = 586.40 \pm 8.92 μm ,

Group C = $597.85 \pm 9.75 \mu\text{m}$, and Group D = $497.82 \pm 7.21 \mu\text{m}$ (Fig. 2d). Global pore size was Group A = $500.80 \pm 10.16 \mu\text{m}$, Group B = $513.74 \pm 6.29 \mu\text{m}$, Group C = $509.90 \pm 6.36 \mu\text{m}$, and Group D = $478.83 \pm 3.38 \mu\text{m}$ (Fig. 2e), confirming global pore size was close to $500 \mu\text{m}$ in all groups.

Assessment of the well-defined local-scale structure

Structural features of local strands, which comprise global strands, were analyzed using optical microscopy (Fig. 3a). Fabricated local strand thickness of the hierarchical scaffolds (Groups A–C) was measured to be $84.35 \pm 8.40 \mu\text{m}$, $82.77 \pm 5.96 \mu\text{m}$, and $88.00 \pm 5.63 \mu\text{m}$, respectively (Fig. 3b). The cross-sectional shape of the strand was determined by the geometry of the extrusion nozzle. In this study, a ceramic circular nozzle was employed, resulting in curved surfaces on the strands. Comparative analysis revealed that the local strand curvature of the scaffolds fabricated in Groups A, B, and C was approximately 6.32 (± 0.44)-fold, 6.14 (± 0.28)-fold, and 5.59 (± 0.45)-fold higher, respectively, than the global strand curvature observed in Group D with a conventional grid-structure (Fig. 3c).

The local pores exhibit two distinct forms, with large-scale (L) and small-scale (S) pores. The measured dimensions of the local pores are as follows: Group A = $205.40 \pm 16.93 \mu\text{m}$ (L) and $149.68 \pm 6.97 \mu\text{m}$ (S), Group B = $184.18 \pm 8.00 \mu\text{m}$ (L) and $114.29 \pm 11.58 \mu\text{m}$ (S), and Group C = $55.55 \pm 4.27 \mu\text{m}$ (S) (Fig. 3d). Comparison of pore size within Groups A and B were statistically significant, highlighting our ability to precisely control

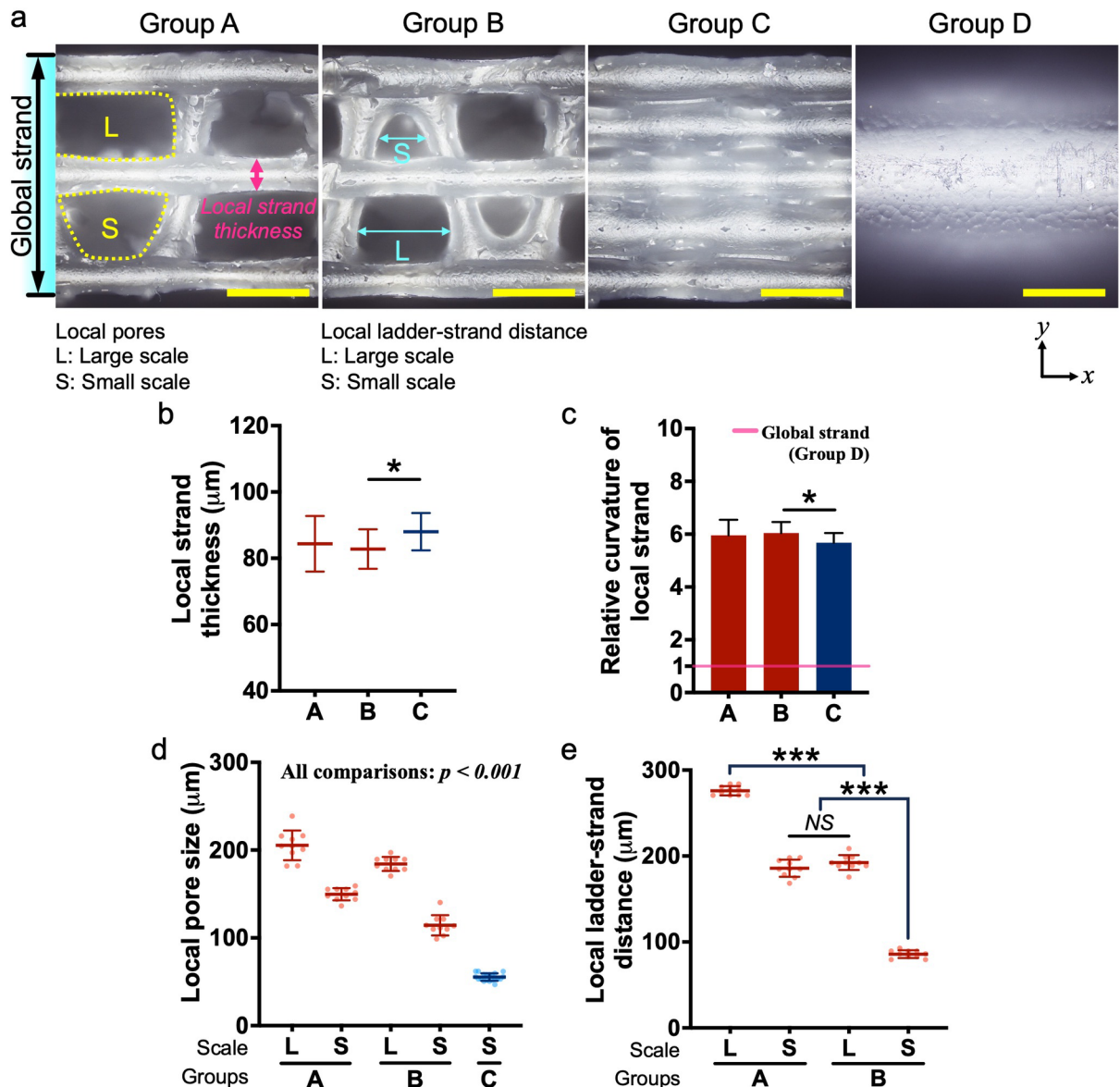


Fig. 3. Fabricated local strand of the scaffold: (a) Optical microscopy images (Top view; $\times 20$; scale bars: $200 \mu\text{m}$); (b) Local strand thickness ($n = 20$), (c) Comparison of the curvature of local strands ($n = 20$), (d) Local pore size (Group A and B: $n = 10$, Group C: $n = 20$), (e) Local ladder-strand distance ($n = 10$; NS: Not significant, * $p < 0.05$, *** $p < 0.001$).

pore size within a single global strand. The ladder strands which span local strands within Groups A and B (as noted in Fig. 3a Group B) were measured for local ladder-strand distance in large-scale (L) and small-scale (S) pores as follows: Group A = $275.93 \pm 5.41 \mu\text{m}$ (L) and $185.82 \pm 9.97 \mu\text{m}$ (S), Group B = $192.40 \pm 8.62 \mu\text{m}$ (L) and $85.77 \pm 4.53 \mu\text{m}$ (S) (Fig. 3e). These results demonstrate our achievement of highly accurate spatial positioning for local pore fabrication with a resolution of $50 \mu\text{m}$. This spatial resolution is essential for precise fabrication of high-quality well-defined hierarchical scaffolds for bone regeneration.

Characteristics of surface wrinkle on the local strand

Group C was designed to have continuous wrinkles by closely controlling the distance between local strands. The fabricated wrinkles on the surface were investigated by 3D laser scanning microscopy. As shown in Fig. 4a, there were significant differences in structure surface area between Groups C and D, while controlled local ladder-strands were observed between Groups A and B. On the top surface (Fig. 4b), the surface roughness in the x-axis for Groups C and D was $1.19 \pm 0.12 \mu\text{m}$ and $0.27 \pm 0.07 \mu\text{m}$ (Fig. 4c), while roughness in the y-axis was $13.43 \pm 1.16 \mu\text{m}$ and $10.76 \pm 0.24 \mu\text{m}$, respectively (Fig. 4d). The surface roughness of Group C in the direction parallel (x-axis) to and perpendicular (y-axis) to the wrinkles was found to be 4.43 times and 1.25 times higher than that of Group D, respectively. The surface roughness in the parallel direction for Groups A and B was $0.96 \pm 0.06 \mu\text{m}$ and $1.01 \pm 0.04 \mu\text{m}$, respectively, showing similar values to that of Group C (Supplementary Fig. S2a). This supports the notion that the local strands in the hierarchical scaffold were fabricated with higher surface roughness than the global strands in Group D. The roughness in the perpendicular direction for Groups A and B was $25.74 \pm 1.12 \mu\text{m}$ and $25.58 \pm 1.05 \mu\text{m}$, respectively, which was higher than that of Group

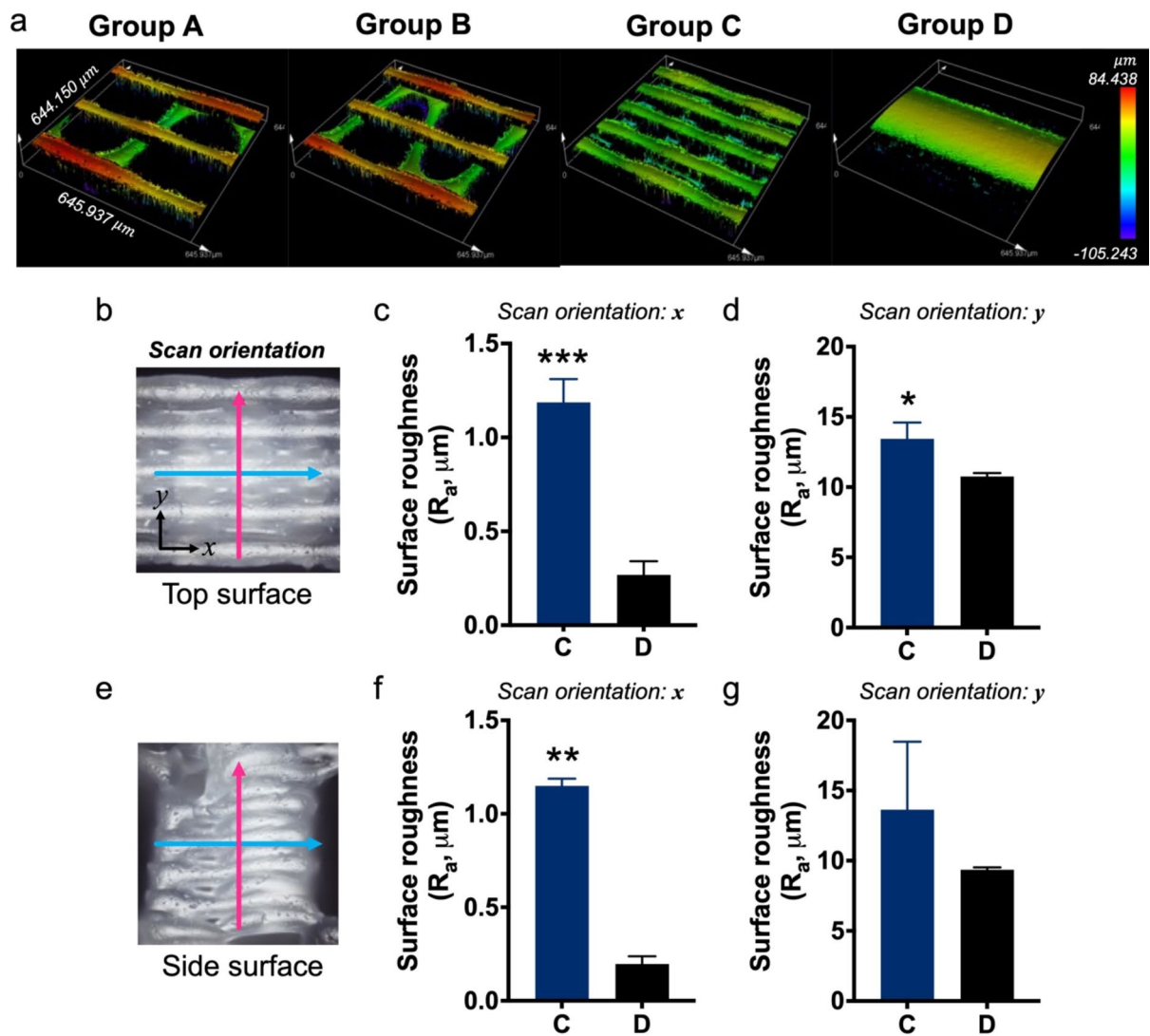


Fig. 4. 3D images of the surface roughness and mean roughness data ($n=3$): (a) 3D surface images, (b) Scan direction on the top surface, (c,d) Surface roughness (R_a) of the x-axis (c) and y-axis (d) on the top surface, (e) Scan direction on the side surface, (f,g) Surface roughness (R_a) of the x-axis (f) and y-axis (g) on the side surface (*: $p < 0.05$, **: $p < 0.01$, ***: $p < 0.001$).

C (Supplementary Fig. S2b). This suggests that adjusting the spacing between local strands can significantly enhance local surface roughness.

On the side surface (Fig. 4e), the surface roughness in the x-axis for Groups C and D was $1.15 \pm 0.04 \mu\text{m}$ and $0.20 \pm 0.04 \mu\text{m}$, while in the y-axis, it was $13.63 \pm 4.84 \mu\text{m}$ and $9.35 \pm 0.17 \mu\text{m}$, respectively (Fig. 4f and g). The surface roughness of Group C in the direction parallel to and perpendicular to the continuous wrinkles was found to be 5.84 times and 1.46 times higher than that of Group D, respectively. In the perpendicular direction, the enhanced surface roughness suggests a synergistic effect of the structurally formed wrinkles from the stacking method and the surface roughness of the local strands. For Groups A and B, surface roughness in the x-axis was $1.46 \pm 0.30 \mu\text{m}$ and $2.02 \pm 0.28 \mu\text{m}$, while in the y-axis, it was $5.58 \pm 1.00 \mu\text{m}$ and $8.06 \pm 0.18 \mu\text{m}$, respectively (Supplementary Figs. S2c and S2d).

Effects of surface topography on hMSC attachment, cytotoxicity, and alignment

As mentioned in Sect. 2.2 to 2.4, the fabricated well-defined hierarchical scaffolds exhibited diverse geometric features based on their fabrication parameters. When used for in vitro cell culture, hMSCs showed excellent adhesion to all scaffold groups, covering most of the local strand surface, and featured many viable cells, as confirmed through live/dead staining images (Fig. 5a). Calcein AM remains inside viable, or live, cells with intact cell membranes and fluoresces green, as seen in Fig. 5b³⁸. In Group A, cells adhered on the local strands and local-ladder strands, leaving the large-scale pores unfilled by cells. In contrast, in Group B, cells were observed to cover most of the local pores, including the large-scale pores. This indicates that adjusting the spacing of the local-ladder strands can effectively regulate cell migration and attachment. Interestingly, on the surface of Group C, cells were arranged either parallel or diagonally along the wrinkles, which contrasts significantly with the cell morphology observed on the surface of Group D, the control group.

In the analysis of cell orientation, the mean cytoskeletal filament orientation of cells in all groups was found to be close to 180° , which may be influenced by the directionality of the global strands (Fig. 5c and d). In Group A, a distinct cell population oriented at 168° (a) was observed, whereas in Group B, cell populations oriented at 135° (b) and 198° (c) were identified (Fig. 5d). This suggests that the cell orientation in Group A is regulated by the ladder-strand, while the cell orientation in Group B can be attributed to the phenomenon of cells covering the local pores. In Group D, cellular populations were identified at 155° (e), 133° (f), and 90° (g), indicating the presence of cells with diverse orientations on the strand surface. In contrast, cells in Group C were distinctly categorized into the 180° direction and 163° (d) direction (Fig. 5d). These findings emphasize that one population aligned along the direction of the wrinkles and while another population aligned on the local strand surface between wrinkles, highlighting a stark contrast to the results observed in Group D. Overall, the comparison of fitted distributions demonstrates the degree of cellular alignment among the groups as follows: Group C > Group A > Group B > Group D (Supplementary Fig. S3). These results support the notion that cellular alignment is regulated by the unique geometric features of the local strands and pore sizes.

The SEM images analyzing the surface clearly revealed cells adhered on the surface of the local strands (Fig. 6a). In Group A, most cells avoided the large pores and migrated toward the local strands, whereas in Group B, cells were observed to align along the local ladder-strands, with their morphology guided in the direction of the global strands (Fig. 6b and c). Notably, the hMSCs can be effectively migrated by the local ladder strands. Elongated cell morphologies were observed during the cell migration process suggesting that, compared to the cell morphology in Group A, the synergistic effect of the appropriately controlled local ladder-strands and the exposed dual-pore structure in Group B plays a significant role in this process. In Group C, many cells were observed to align along the continuous wrinkles, which contrasts sharply with Group D. This finding was also significantly different compared to Groups A and B, where the pores were distinctly exposed.

Discussion

Recently, fabrication of hierarchical scaffolds using biopolymers have been described through various distinct methods and materials. Ghosh et al.³⁹ developed 3D printed hierarchical porous PCL scaffolds using Pickering high internal phase emulsion (HIPE) templates, which enabled precise control over pore structure. This method generated interconnected macroporous structures with tunable porosity, enhancing scaffold performance in load-bearing tissue engineering applications by providing high mechanical stability and excellent cell permeability. Dai et al.⁴⁰ developed hierarchical porous calcium-deficient hydroxyapatite (CDHA) scaffolds using indirect 3D printing, aiming to enhance osteogenesis and bone regeneration. These scaffolds exhibited a biomimetic architecture with multi-scale porosity, facilitating cell adhesion, proliferation, and osteogenic differentiation. Lu et al.⁴¹ developed a β -TCP ceramic scaffold with a hierarchical pore structure using 3D printing and porogen-based techniques to enhance osteogenesis and bone defect repair. The scaffold exhibited optimized porosity and mechanical properties, promoting cell adhesion, proliferation, and osteogenic differentiation. These results demonstrate that hierarchical scaffolds can be utilized for a variety of applications by integrating structural and material strategies to best suit particular contexts. They also suggest that techniques for fabricating irregular micropores are still widely used. In this study, hierarchical structured scaffolds were successfully fabricated using PED head printing high-resolution technology, and the impact of the well-defined local micro-environment on human MSC behavior was investigated. Our findings provide potential insights into the role of well-defined scaffold microenvironments and geometries in guiding cell alignment and promoting successful osteogenic differentiation embedded cells.

To design a well-defined strand hierarchy, we introduced the concept of a “scaffold in a scaffold” based on an easily definable grid-structure design. As shown in Fig. 1, we established an optimal definition for the local strand building blocks and fabricated a novel design through controlling its three-dimensional arrangement. This approach provides a clear and systematic framework for investigating the influence of hierarchical structures on cellular responses and scaffold functionality. To achieve this, we defined and characterized the 3D geometry of

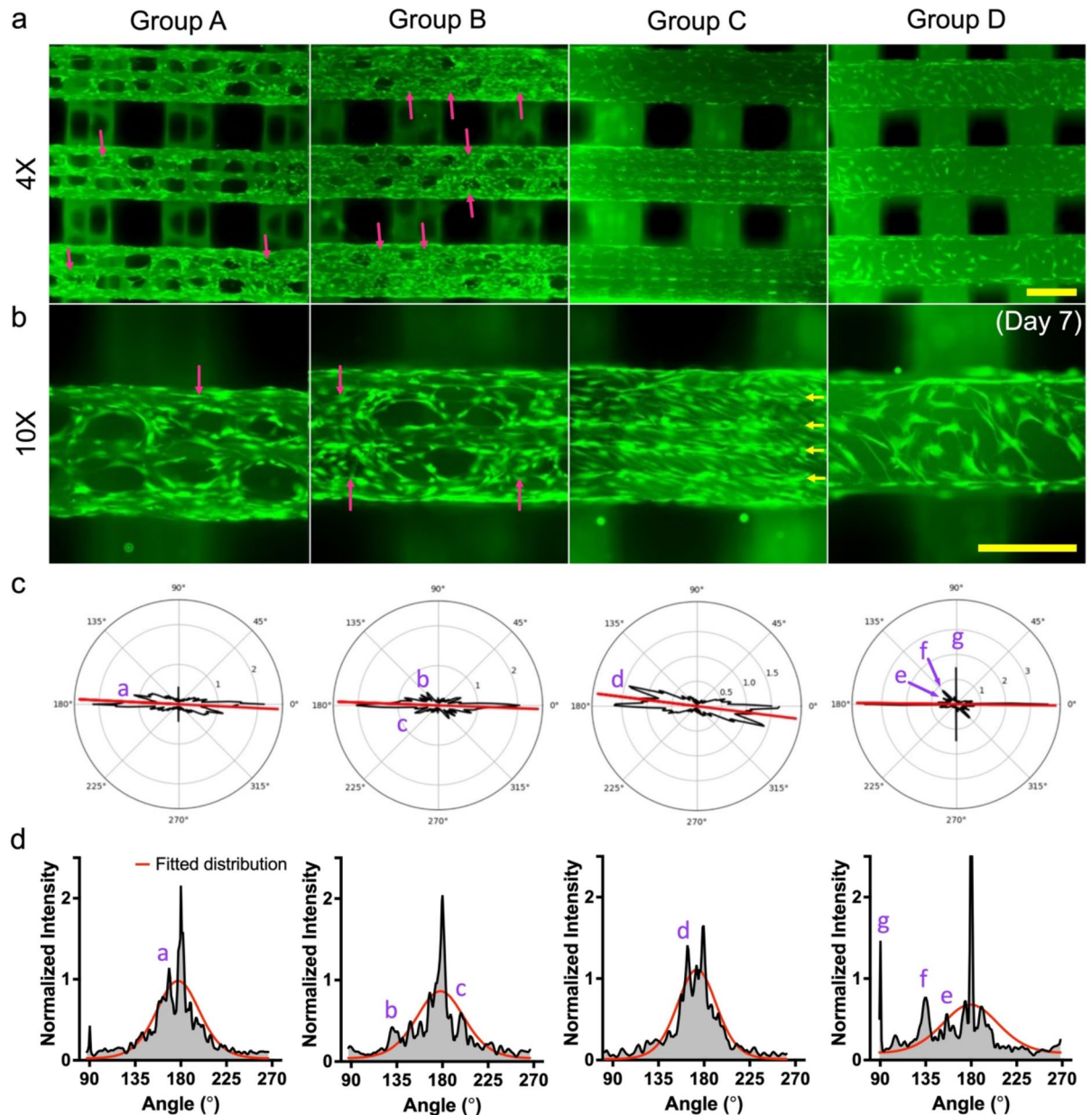


Fig. 5. Cytotoxicity and cellular morphology: Live/dead stain images of hMSCs cultured for 7 days: (a) $\times 4$, (b) $\times 10$ (red arrows: cells covering the pores, yellow arrows: Continuous wrinkle line; Scale bars: 500 μm), (c) Polar plot of normalized power intensity (Red line: mean fibril orientation; Letter indicators: local peak values), (d) Cartesian plot of the normalized power intensity (Letter indicators: Corresponding points from the previous polar plot peak values) with the best-fit semicircular von Mises distribution (Red curve).

the local strands and pores in multiple geometric configurations. Notably, the fabricated hierarchical scaffolds (Group A and B) demonstrated over 30% higher porosity compared to the conventional scaffold (Group D), despite having a global strand thickness approximately 100 μm greater (Fig. 2c and d).

The three-dimensional hierarchical scaffold, fabricated using PED head printing technology, is composed of a continuous 3D structure of thin PCL strands. This design provides cell attachment sites with significantly high curvature and surface roughness, offering a unique structural environment and promoting cell adhesion (Fig. 3b and c, and 4c). Others have shown how high surface roughness contributes to cell attachment and proliferation⁴², and macroscale substrates with radii of curvature ranging from tens to hundreds of micrometers are known to influence cellular morphology and stress fiber alignments⁴³. These previous reports support our findings that the controlled local strand patterns in the fabricated hierarchical scaffold can guide cell migration and alignment.

Moreover, this fabrication method enabled the precise spatial patterning of local strands within scaffolds, allowing for the modulation of local pore size and the formation of aligned wrinkled surfaces (Fig. 4a). These controlled strand patterns within the hierarchical structure provided a unique microenvironment that influenced

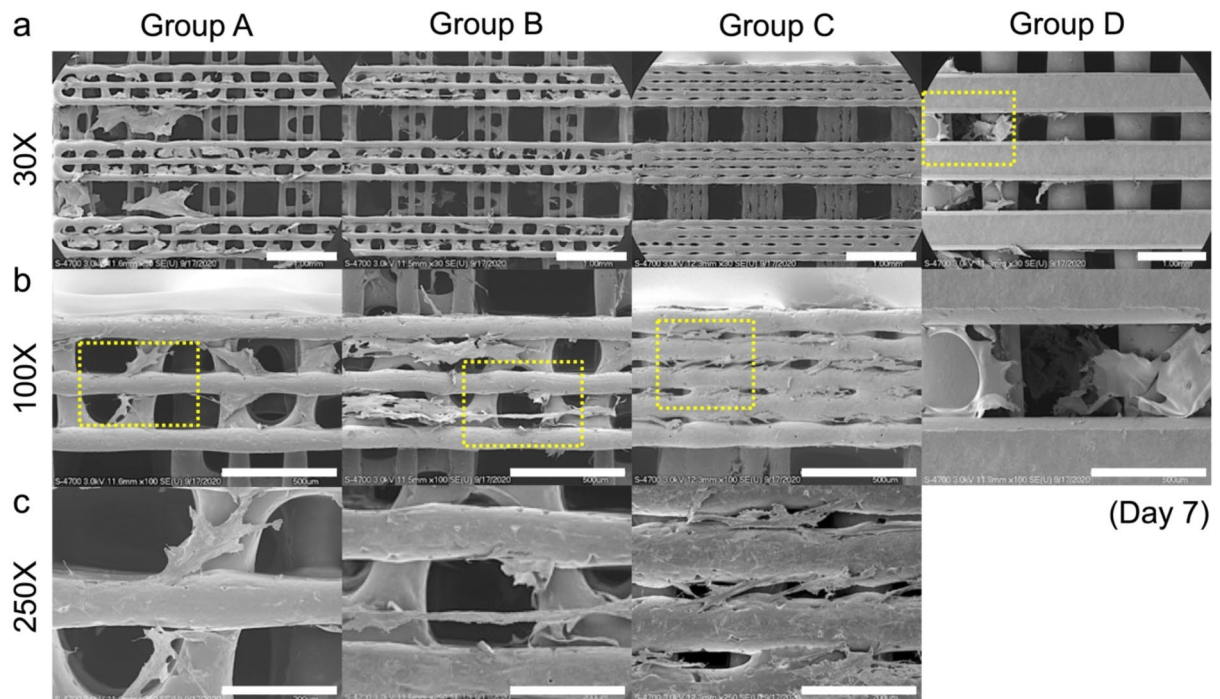


Fig. 6. FE-SEM images of attached hMSCs on the scaffold surface (Day 7): (a) $\times 30$ (Scale bars: $1000 \mu m$), (b) $\times 100$ (Scale bars: $500 \mu m$), and (c) $\times 250$ (Scale bars: $200 \mu m$).

cellular behavior. Through in vitro cell culture experiments, we confirmed that the designed patterns effectively altered the migration and alignment of human MSCs, as illustrated in Fig. 7. Kosik-Kozioł et al. introduced the results of stimulating osteogenesis by changing the microporosity of PCL fibers using ultrasonic stimulation in acetone and NaOH solvents⁴⁴. These results imply that precisely controlled local strand patterns provide geometries that play a crucial role in regulating cell morphology and cytoskeletal organization, potentially influencing MSC differentiation. Further, these functional characteristics of our developed scaffold pose great potential for the regeneration of tissues with explicit cell alignment properties. For example, the tendon-bone interface (TBI) is highly anisotropic, consisting of mechanical, compositional, and hierarchical structures resembling both tendon and bone⁴⁵, with tendons being particularly dependent on cell and tissue alignment⁴⁶. Electrospinning technology has long been used for tendon/ligament regeneration by inducing cell alignment with aligned nanofibers⁴⁷, but this approach still has limitations in fabricating three-dimensionally thick or large volumes. Our hierarchical scaffold has the advantage of being able to produce large 3D volumes and fabricate gradient structures from bone tissue to soft tissue, while simultaneously inducing cell alignment.

The solvent-free 3D printing method using PED head printing used here provides improved in vivo safety measured during scaffold implantation compared to contemporary methods. However, limitations associated with this method still persist. The increased head pathway necessary to form the architecture of the local strand patterns remains a challenge, as this extends scaffold fabrication times. Similarly, given the significance of scaffold mechanics in tissue engineering applications, the lack of mechanical performance evaluation remains a limitation of this study and should be addressed in future research. Moreover, long term in vitro culture and animal tests will be required for clinical translation. Currently, our optimized PCL scaffold with a well-defined hierarchical structure holds great potential to be excellent for safety and to support effective tissue regeneration for various tissues in clinical applications. Overall, the findings in this study underscore the importance of hierarchical design in scaffolds for directing cellular organization and behavior, which is critical for advancing tissue engineering strategies. Future studies should include various in vitro tests, such as transcriptional analysis, and animal experiments to verify in vivo safety and functionality.

Methods

Materials

PCL ($M_n = 45,000$, $T_m = 60^\circ C$, Polysciences, USA) was used for the fabrication of the biocompatible scaffold. A digital scale (AB204-S, Mettler Toledo, Switzerland) with 0.1 mg resolution was used for measurement of weight of scaffold.

For in-vitro culture, human mesenchymal stem cells (hMSCs) and mesenchymal stem cell growth medium (MSCGM; Supplement kit for proliferation of human bone marrow-derived mesenchymal stem cells) were purchased from Lonza (Switzerland)⁴⁸. All cells were cultured at CO₂ incubator (5% CO₂, 37 °C). The medium was refreshed every 2–3 days.

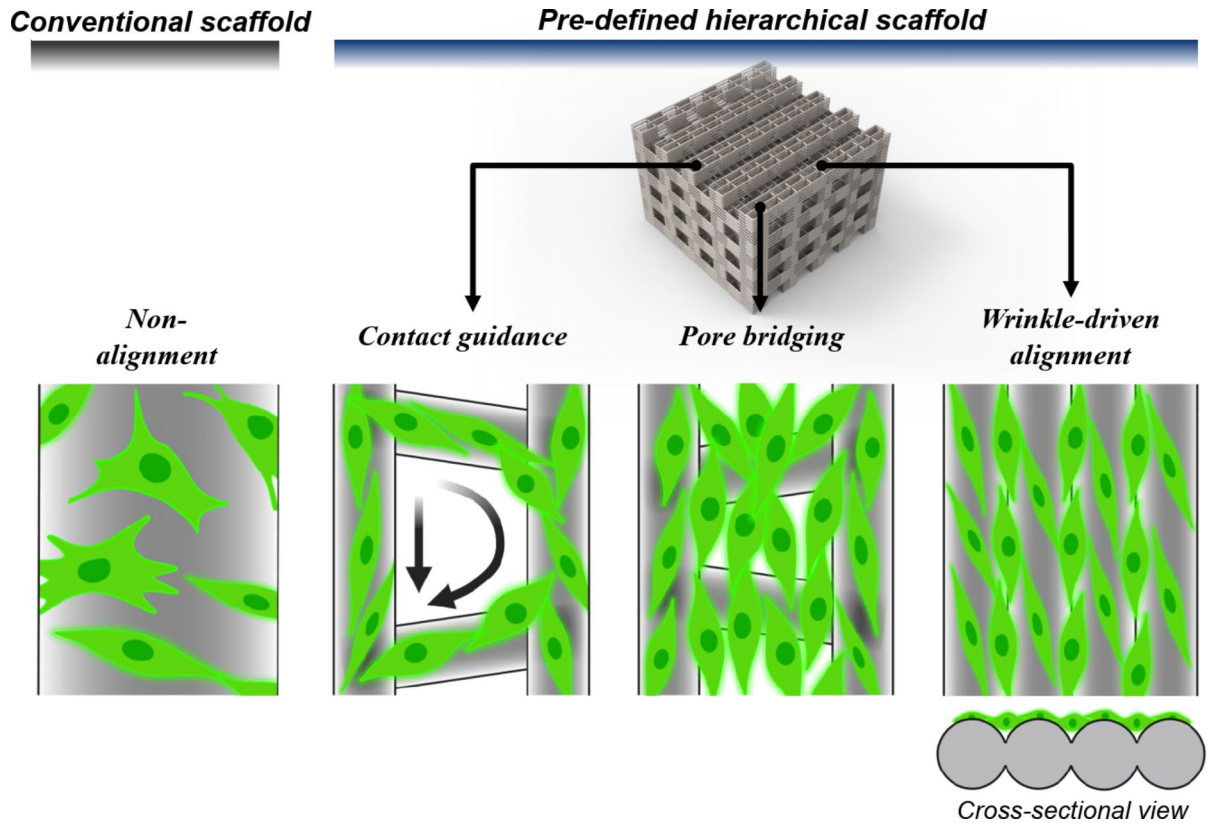


Fig. 7. Illustration of the cellular morphology induced by predefined local strands of the well-defined hierarchical scaffold (This figure was partially created with BioRender.com; <https://BioRender.com/p97x133>).

	In a local strand		
	Local ladder-strand distance (μm)	N_{long} (n)	N_{short} (n)
Group A	357	27	3
Group B	250	21	3
Group C	192	15	5

Table 2. Predefined dimensions based on tool pathway in a local strand.

Precision 3D printing technology with PED head system

Representative design parameters were defined to fabricate a global strand (Fig. 1a). To generate a tool pathway, an in-house software developed with Visual Basic 6.0 (Microsoft, USA) was used to generate g-code (Supplementary Fig. S4). The exterior dimensions of scaffold were designed with $5.0 \text{ mm} \times 5.0 \text{ mm} \times 2.7 \text{ mm}$ ($L \times W \times H$). Dimensions to design a 3D porous global strand of well-defined hierarchical scaffold were predefined as follow: $W_{local\ strand} = 500 \mu\text{m}$, $L_y = 5,000 \mu\text{m}$, and $h_{layer} = 50 \mu\text{m}$. The design parameters differing by group followed those listed in Table 2.

The lab-made precision 3D printer with the PED head system was used for fabrication¹⁷. PCL pellets were melted in the printer barrel at $90 \text{ }^\circ\text{C}$ and then extruded by rotating the screw at 25 rpm under an air pressure of $255 \pm 5 \text{ kPa}$. The hierarchical scaffolds with controlled pores were fabricated using a $50 \mu\text{m}$ ceramic nozzle. As an ordinary design, a grid-structure scaffold was fabricated using a $400 \mu\text{m}$ ceramic nozzle and used for a control group (Group D).

Characterization of fabricated 3D scaffold

Optical microscopy images of the scaffold surface were obtained using a 3D laser scanning microscope (OLS5100; Olympus, Japan) in the laser field mode with objective lenses MPLAPON20 \times LEXT to observe pore size of the fabricated scaffold.

Equation (1) was used to define the pore size of the scaffold as follows.

$$\text{Pore size } (\mu\text{m}) = \frac{(L_v + L_h)}{2} \quad (1)$$

where L_v and L_h are the lengths of the pore measured in the vertical and horizontal direction, respectively. The pore size was calculated by averaging the L_v and L_h values ($n=5$) measured by the optical microscope.

Equation (2) was used to calculate the porosity of the scaffold as follows.

$$\text{Porosity (\%)} = \frac{(V_0 - (\frac{m_s}{\rho_{PCL}}))}{V_0} \times 100 \quad (2)$$

Where V_0 defines the calculated volume from the apparent dimensions of scaffold in disregard of pores. m_s and ρ_{PCL} are the mass of the scaffold and the density of the PCL material (1.145 g cm^{-3}).

The local filament curvature was the reciprocal of the filament radius. Global strand curvature of the Group D was used as an arbitrary curvature reference value for the global strand, and the average of the 10 measured values was used. Average value of the 20 measured thickness of the Groups A-C as local strand was used for the calculation.

Surface topology characterization by 3D laser scanning microscope

To investigate the surface roughness generated by deposition method, 3D topography profiles on the surface were measured using the 3D laser scanning microscope (OLS5100) in the laser field mode with objective lenses MPLAPON20 \times LEXT, and a working distance of 0.60 mm.

Line roughness profiles of the fabricated scaffold were determined via a 3D laser scanning microscope, where average roughness values (R_a) were determined according to an Equation (3).

$$R_a = \frac{1}{l} \int_0^l |z(x)| dx \quad (3)$$

Where ' l ' is the evaluation length, and ' $z(x)$ ' means the profile height function. Five scaffolds per group were used for analysis⁴⁹.

Evaluation of cell viability and cytoplasm orientation

The fabricated scaffolds underwent disinfection by rinsing with a 70% ethanol solution and sterilization by exposure to UV light for 30 min. After that, the scaffolds were soaked in the culture medium for 1 h⁵⁰. The seeding density of hMSCs was determined through preliminary tests (**Supplementary Fig. S5**). The hMSCs were seeded on a scaffold at a density of 2×10^5 cells (Passage 3). After that, the scaffold was cultured in the incubator for 7 days. The medium was refreshed every 2–3 days. After 7 days, cell viability was assessed using the Live/dead Kit (Invitrogen, USA). Live cells were stained by a Calcein acetoxymethyl (Calcein-AM) and dead cells were stained by an Ethidium homodimer-1. Live and dead cells were examined by fluorescence microscopy (Eclipse Ti2, Nikon, Japan). Furthermore, a semicircular von Mises distribution computed using FiberFit was performed to analyze the cytoplasm alignment stained by the calcein AM⁵¹.

Scanning electron microscopy

For sample preparation, the hierarchical scaffold with attached cells was fixed with 1% osmium tetroxide at 4 °C for an hour. After undergoing standard ethanol serial dehydration, the samples were freeze-dried using a freeze dryer (ES-2030, Hitachi, Japan) and coated with platinum using an ion coater (IB-5, Eiko, Japan). The samples were then examined with a scanning electron microscope (S-4700, Hitachi, Japan).

Statistical analysis

All data were indicated as the mean \pm standard deviation. Statistical analysis was performed using one-way ANOVA with Tukey's post hoc testing, applying a 95% confidence interval via GraphPad version 9 software (Prism, USA). A p -value of less than 0.05 was considered statistically significant.

Conclusion

In this study, we successfully fabricated PCL scaffolds with well-defined hierarchical structure by a solvent-free additive manufacturing approach. By precisely controlling the local strand patterns within the scaffold, we identified key features important for 3D polymeric scaffolds to regulate the human MSC migration and morphology. The hierarchical structure facilitated spatial guidance of the cells, demonstrating the influence of strand geometry and arrangement on cellular behavior. These findings highlight the strong potential of engineered scaffold designs in directing cellular organization, a crucial step for achieving functional tissue regeneration. Such control over cellular behavior can open opportunities for the development of advanced biomaterials tailored to specific regenerative medicine applications, offering a novel strategy for the advancement of tissue engineering.

Data availability

The datasets generated during and/or analyzed during the current study are available from the corresponding author upon reasonable request.

Received: 3 February 2025; Accepted: 25 March 2025

Published online: 04 April 2025

References

- Lee, S. S., Du, X., Kim, I. & Ferguson, S. J. Scaffolds for bone-tissue engineering. *Matter* **5**, 2722–2759 (2022).
- Rioja, A. Y., Daley, E. L. H., Habif, J. C., Putnam, A. J. & Stegemann, J. P. Distributed vasculogenesis from modular agarose-hydroxyapatite-fibrinogen microbeads. *Acta Biomater.* **55**, 144–152 (2017).
- Keating, J. F., Simpson, A. H. R. W. & Robinson, C. M. The management of fractures with bone loss. *J. Bone Joint Surg. Br. Volume 87-B*, 142–150 (2005).
- Annamalai, R. T. et al. Injectable osteogenic microtissues containing mesenchymal stromal cells conformally fill and repair critical-size defects. *Biomaterials* **208**, 32–44 (2019).
- Liang, J. et al. Study on the fabrication and performance of hierarchical porous 3D printed PCL-based artificial bone scaffold with anti-bacterial effect. *Mater. Today Commun.* **39**, 108637 (2024).
- Xue, N. et al. Bone tissue engineering in the treatment of bone defects. *Pharmaceuticals* **15**, 879 (2022).
- Reichert, J. C. et al. A tissue engineering solution for segmental defect regeneration in Load-Bearing long bones. *Sci. Transl. Med.* **4**, 141ra93–141ra93 (2012).
- Yasmeen, S., Lo, M. K., Bajracharya, S. & Roldo, M. Injectable scaffolds for bone regeneration. *Langmuir* **30**, 12977–12985 (2014).
- Lee, S. H. et al. Evaluation of mechanical strength and bone regeneration ability of 3D printed kagome-structure scaffold using rabbit calvarial defect model. *Mater. Sci. Engineering: C*, **98**, 949–959 (2019).
- Gharibshahian, M. et al. Recent advances on 3D-printed PCL-based composite scaffolds for bone tissue engineering. *Front. Bioeng. Biotechnol.* **11**, (2023).
- Bertsch, C. et al. Biomimetic bilayered scaffolds for tissue engineering: from current design strategies to medical applications. *Adv. Healthc. Mater.* **12**, 2203115 (2023).
- Chan, B. P. & Leong, K. W. Scaffolding in tissue engineering: general approaches and tissue-specific considerations. *Eur. Spine J.* **17**, 467–479 (2008).
- Lee, S. H., Lee, J. H. & Cho, Y. S. Analysis of degradation rate for dimensionless surface area of well-interconnected PCL scaffold via in-vitro accelerated degradation experiment. *Tissue Eng. Regen Med.* **11**, 446–452 (2014).
- Bose, S., Roy, M. & Bandyopadhyay, A. Recent advances in bone tissue engineering scaffolds. *Trends Biotechnol.* **30**, 546–554 (2012).
- Egan, P. F., Ferguson, S. J. & Shea, K. Design of hierarchical Three-Dimensional printed scaffolds considering mechanical and biological factors for bone tissue engineering. *J. Mech. Des.* **139**, (2017).
- Pei, M., Hwangbo, H. & Kim, G. Fabrication of 3D-printed coiled PCL microfibrillar bundles using alginate-based biocomposites for bone tissue engineering applications. *Int. J. Extrem. Manuf.* **7**, 025501 (2024).
- Javaid, M., Haleem, A., Singh, R. P. & Suman, R. 3D printing applications for healthcare research and development. *Global Health J.* **6**, 217–226 (2022).
- Ng, W. L., An, J. & Chua, C. K. Process, material, and regulatory considerations for 3D printed medical devices and tissue constructs. *Engineering* **36**, 146–166 (2024).
- Brooks, A. K. & Yadavalli, V. K. Post-Print processing to minimize cytotoxicity of 3D-Printed photopolymer resins for biomedical applications. *J. Appl. Polym. Sci.* **142**, e56545 (2025).
- Mohanty, S. et al. Fabrication of scalable tissue engineering scaffolds with dual-pore microarchitecture by combining 3D printing and particle leaching. *Mater. Sci. Eng. C* **61**, 180–189 (2016).
- Khademhosseini, A., Vacanti, J. P. & Langer, R. Progress in tissue engineering. *Sci. Am.* **300**, 64–71 (2009).
- Wray, L. S. et al. A silk-based scaffold platform with tunable architecture for engineering critically-sized tissue constructs. *Biomaterials* **33**, 9214–9224 (2012).
- Kenar, H., Köse, G. T. & Hasirci, V. Tissue engineering of bone on micropatterned biodegradable polyester films. *Biomaterials* **27**, 885–895 (2006).
- Gu, J. et al. Hierarchical engineering scaffolds for oral and craniofacial tissue regeneration: recent advances and challenges. *Appl. Mater. Today* **42**, 102546 (2025).
- Minardi, S. et al. Evaluation of the osteoinductive potential of a bio-inspired scaffold mimicking the osteogenic niche for bone augmentation. *Biomaterials* **62**, 128–137 (2015).
- Lemos, R., Maia, F. R., Reis, R. L. & Oliveira, J. M. Engineering of extracellular Matrix-Like biomaterials at Nano- and macroscale toward fabrication of hierarchical scaffolds for bone tissue engineering. *Adv. NanoBiomed Res.* **2**, 2100116 (2022).
- Aghaiee, S., Azdast, T., Hasanzadeh, R. & Farhangpazhouh, F. Fabrication of bone tissue engineering scaffolds with a hierarchical structure using combination of 3D printing/gas foaming techniques. *J. Appl. Polym. Sci.* **141**, e55238 (2024).
- Choi, W. J. et al. Rapid development of dual porous poly(lactic acid) foam using fused deposition modeling (FDM) 3D printing for medical scaffold application. *Mater. Sci. Eng. C* **110**, 110693 (2020).
- Luo, B. et al. An Encapsulation-Free and hierarchical porous triboelectric scaffold with dynamic hydrophilicity for efficient cartilage regeneration. *Adv. Mater.* **36**, 2401009 (2024).
- Kang, N. U., Hong, M. W., Kim, Y. Y., Cho, Y. S. & Lee, S. J. Development of a powder extruder system for Dual-pore Tissue-engineering scaffold fabrication. *J. Bionic Eng.* **16**, 686–695 (2019).
- Camarero-Espinosa, S. et al. 3D printed Dual-Porosity scaffolds: the combined effect of stiffness and porosity in the modulation of macrophage polarization. *Adv. Healthc. Mater.* **11**, 2101415 (2022).
- Sohn, D. G., Hong, M. W., Kim, Y. Y. & Cho, Y. S. Fabrication of Dual-pore scaffolds using a combination of Wire-Networked molding (WNM) and Non-solvent induced phase separation (NIPS) techniques. *J. Bionic Eng.* **12**, 565–574 (2015).
- Cho, Y. S. et al. Fabrication of dual-pore scaffolds using SLUP (salt leaching using powder) and WNM (wire-network molding) techniques. *Mater. Sci. Eng. C* **45**, 546–555 (2014).
- Feng, X. et al. Influence of pore architectures of silk fibroin/collagen composite scaffolds on the regeneration of osteochondral defects *in vivo*. *J. Mater. Chem. B*, **8**, 391–405 (2020).
- Baker, B. M. & Mauck, R. L. The effect of nanofiber alignment on the maturation of engineered meniscus constructs. *Biomaterials* **28**, 1967–1977 (2007).
- Baker, B. M., Nathan, A. S., Gee, A. O. & Mauck, R. L. The influence of an aligned nanofibrous topography on human mesenchymal stem cell fibrochondrogenesis. *Biomaterials* **31**, 6190–6200 (2010).
- Mathieu, P. S. & Lobo, E. G. Cytoskeletal and focal adhesion influences on mesenchymal stem cell shape, mechanical properties, and differentiation down osteogenic, adipogenic, and chondrogenic pathways. *Tissue Eng. Part. B: Reviews*, **18**, 436–444 (2012).
- Gutiérrez, L. et al. Nanotechnology in drug discovery and development. <https://doi.org/10.1016/B978-0-12-409547-2.12311-X> (2017).
- Ghosh, S. et al. 3D printed hierarchical porous Poly(ϵ -caprolactone) scaffolds from Pickering high internal phase emulsion templating. *Langmuir* **39**, 1927–1946 (2023).
- Dai, W. et al. Indirect 3D printing CDHA scaffolds with hierarchical porous structure to promote osteoinductivity and bone regeneration. *J. Mater. Sci. Technol.* **207**, 295–307 (2025).
- Lu, T., Liang, Y., Zhang, L., Yuan, X. & Ye, J. Fabrication of β -TCP ceramic scaffold with hierarchical pore structure using 3D printing and Porogen: investigation of osteoinductive and bone defects repair properties. *Appl. Mater. Today* **40**, 102351 (2024).
- Gupta, D., Singh, A. K., Kar, N., Dravid, A. & Bellare, J. Modelling and optimization of NaOH-etched 3-D printed PCL for enhanced cellular attachment and growth with minimal loss of mechanical strength. *Mater. Sci. Engineering: C* **98**, 602–611 (2019).

43. Bade, N. D., Kamien, R. D., Assoian, R. K. & Stebe, K. J. Curvature and Rho activation differentially control the alignment of cells and stress fibers. *Sci. Adv.* **3**, e1700150 (2017).
44. Kosik-Kozioł, A. et al. Surface modification of 3D printed Polycaprolactone constructs via a solvent treatment: impact on physical and osteogenic properties. *ACS Biomater. Sci. Eng.* **5**, 318–328 (2019).
45. Dong, Y. et al. Structure, ingredient, and function-based biomimetic scaffolds for accelerated healing of tendon-bone interface. *J. Orthop. Translation.* **48**, 70–88 (2024).
46. Yin, H. et al. The essential role of aligned architecture in decellularized tendon matrix mediated stem cell tenogenic differentiation and tendon repair. *Polym. Test.* **132**, 108378 (2024).
47. Liang, C. et al. Electrospinning technology: a promising approach for tendon–bone interface tissue engineering. *RSC Adv.* **14**, 26077–26090 (2024).
48. Balachander, G. M., Nilawar, S., Meka, S. R. K., Ghosh, L. D. & Chatterjee, K. Unravelling MicroRNA regulation and miRNA–mRNA regulatory networks in osteogenesis driven by 3D nanotopographical cues. *Biomater. Sci.* **12**, 978–989 (2024).
49. Lee, S. H. et al. Mechanical properties and cell-culture characteristics of a Polycaprolactone kagome-structure scaffold fabricated by a precision extruding deposition system. *Biomed. Mater.* **12**, 055003 (2017).
50. Shor, L. et al. Precision extruding deposition (PED) fabrication of Polycaprolactone (PCL) scaffolds for bone tissue engineering. *Biofabrication* **1**, 015003 (2009).
51. Morrill, E. E. et al. A validated software application to measure fiber organization in soft tissue. *Biomech. Model. Mechanobiol.* **15**, 1467–1478 (2016).

Acknowledgements

We sincerely thank Felicia R. Pinto (University of Pennsylvania, United States) and Tyler Blanch (University of Pennsylvania, United States) for their constructive feedback on the manuscript. This work was supported by a National Research Foundation of Korea (NRF) grant funded by the Korean government (No. RS-2024-00344151).

Author contributions

All experiments and manuscript preparation are designed by S.-H. Lee. S.-H. Lee and N.-U. Kang performed experiments to fabricate samples. S.-H. Lee and Y. S. Cho performed the characterization of samples. J. Lee conducted the cell culture experiments. S. C. Heo reviewed and revised all of the manuscripts. Y. Park and Y.-S. Cho supervised and revised all of the manuscript.

Declarations

Competing interests

The authors declare no competing interests.

Additional information

Supplementary Information The online version contains supplementary material available at <https://doi.org/10.1038/s41598-025-96027-1>.

Correspondence and requests for materials should be addressed to Y.P. or Y.-S.C.

Reprints and permissions information is available at www.nature.com/reprints.

Publisher's note Springer Nature remains neutral with regard to jurisdictional claims in published maps and institutional affiliations.

Open Access This article is licensed under a Creative Commons Attribution-NonCommercial-NoDerivatives 4.0 International License, which permits any non-commercial use, sharing, distribution and reproduction in any medium or format, as long as you give appropriate credit to the original author(s) and the source, provide a link to the Creative Commons licence, and indicate if you modified the licensed material. You do not have permission under this licence to share adapted material derived from this article or parts of it. The images or other third party material in this article are included in the article's Creative Commons licence, unless indicated otherwise in a credit line to the material. If material is not included in the article's Creative Commons licence and your intended use is not permitted by statutory regulation or exceeds the permitted use, you will need to obtain permission directly from the copyright holder. To view a copy of this licence, visit <http://creativecommons.org/licenses/by-nc-nd/4.0/>.

© The Author(s) 2025